Elaborate simulations and forecasting of the effects of urbanization on karst flood events using the improved Karst-Liuxihe model

Ji Li[a,*], Aihua Hong[b], Daoxian Yuan[a,c], Yongjun Jiang[a], Yuanzhu Zhang[a,*], Shujin Deng[b], Cong Cao[b], Jiao Liu[d], Yangbo Chen[e]

[a] School of Geographical Sciences of Southwest University, Chongqing Key Laboratory of Karst Environment, Chongqing 400715, China
[b] The Laboratory of Chongqing Groundwater Resource Utilization and Environmental Protection (Nanjiang Hydrogeological Team Under the Chongqing Geological Bureau of Geology and Minerals Exploration), Chongqing 401121, China
[c] Karst Dynamic Laboratory, Ministry of Land and Resources, Guilin 541004, China
[d] Chongqing Hydrology and Water Resources Bureau, Chongqing 401120, China
[e] Department of Water Resources and Environment, Sun Yat-sen University, Guangzhou 510275, China

ARTICLE INFO

ABSTRACT

Urbanization, especially land use pattern changes, has a great impact on natural flood events in a karst basin. Quantitative simulations of the effects of urbanization on karst flood events and forecasts of future evolution trends are difficult based on the current hydrological models. These models often require a large amount of data when used in karst areas due to the complex model structure and model parameters. To overcome the limitations of model applications, a physically based and fully distributed karst hydrological model, i.e., the improved Karst-Liuxihe (IKL) model, was proposed in this study to simulate and forecast karst flood events under the influence of urbanization. This IKL model was developed through the overall improvement of the Karst-Liuxihe (KL) model. The main additions were the improved runoff generation algorithm and the underground river confluence module. The karst flood simulation results of the IKL model were much better than those of the KL model: the average values of the Nash–Sutcliffe coefficient, correlation coefficient, and coefficient of the water balance increased by 23%, 23% and 26%, respectively, while the process relative error, flood peak flow relative error, and flood peak flow time error decreased by 21%, 22%, and 3 h, respectively, which confirmed that the improvements to the model were effective and feasible. Therefore, this paper used the IKL model to simulate karst flood events and annual runoff under the influence of urbanization based on 4 extreme land use scenarios. In addition, the model effectively forecasted the future runoff in 2030, 2040, and 2050. The results indicated that the critical proportion of urbanized area throughout the watershed area was 45%. When the urban proportion exceeded 45%, waterlogging could occur in the study area.

1. Introduction

Human activities associated with urban development have had a considerable effect on the climate and environment. In particular, the development and utilization of land have caused dramatic changes in the global environment over the past several decades (Rao, 2005). To study the impacts of human activities on environmental changes, the International Geosphere-Biosphere Program (IGBP) and International Human Dimensions Programme (IHDP) proposed a research project focused on land use/land cover change (LUCC) in 1994, and research on LUCC has become popular (Turner et al., 1990; Meyer and Turner, 1994). Studies on the hydrological effects of urbanization, especially LUCC, are necessary to identify the important impacts on floods and

water resources in karst watersheds (Frumkin, 2002; Trcek et al., 2006; Zhu and Li, 2014; Bittner et al., 2018).

In general, the carrying capacity of the eco-environment in karst areas is low, and the environmental effects of urbanization are prominent. The LUCC during urbanization processes can greatly increase the impermeable area and change the spatial and temporal patterns of the surface runoff and water balance conditions (Yuan, 2002; Cornaton and Perrochet, 2002; Hartmann et al., 2014; Bittner et al., 2018). Moreover, karst landforms can change under the influence of LUCC and the hydrological process of rainfall infiltration. The main manifestations of these changes are increases in the peak discharge and runoff volume, a sharpened and steepened discharge hydrograph, reduced surface infiltration, and an increased likelihood of catastrophic flooding (Cao,

2012; Lan, 2014; Hartmann et al., 2015). Therefore, it is critical to simulate and forecast regional floods to reduce flood losses in karst basins.

This paper selected the Laolongdong karst watershed in Southwest China as an example and conducted an impact analysis of urbanization on flood events and annual runoff in a karst area. The Laolongdong karst cave is a famous tourist attraction, and many tourists are attracted by the cave's reputation. In recent years, the research area has undergone rapid urbanization, marked increases in urban areas, and drastic changes in land use patterns, which have greatly changed the natural underlying surface conditions. The unreasonable urbanization-based development plan has had a negative hydrological effect. This effect is manifested in the dramatic increase in impermeable area, which results in a decrease in seepage and frequent urban waterlogging. With the increase in urbanization in the study area, several catastrophic floods have occurred in recent years (Zhang, 2017). For example, Fairy Dong, once a famous tourist attraction, was closed after repeated waterlogging incidents. Therefore, it is necessary to simulate and evaluate the hydrological effects of urbanization and discuss how increases in the built-up land area due to urbanization can lead to waterlogging disasters in karst areas. A hydrological model could be a promising tool for studying the impact of urbanization on karst flood events (Bittner et al., 2018; Bhave et al., 2018).

The current commonly used hydrological models in karst areas mainly focus on solving problems related to water resource management or water environment assessments, and quantitative model research on the hydrological effects of urbanization is lacking (Nikolaidis et al., 2013; Hartmann et al., 2014, 2015; Li et al., 2019a, b). Quantitative calculations of this effect using the currently available hydrological models and accurate predictions of future hydrological evolutionary trends are difficult (McMahon et al., 2008; Hartmann et al., 2015; Sarrazin et al., 2018). Traditional hydrological models, such as lumped models, have some shortcomings in applications in karst areas due to their simple structure (Dewandel et al., 2003; Bittner et al., 2018), and emphasis is placed on the input and output of the model (Liedl et al., 2003). The karst hydrological processes in the middle are often uncertain in these lumped models (Hartmann et al., 2015). Thus, these traditional lumped hydrological models may not be applicable for evaluating the effect of urbanization on flood events in karst areas (Fleury et al., 2007; Geyer et al., 2008).

Distributed hydrological models have the potential to improve the accuracy of karst flood simulations (Ambroise et al., 1996; Zhu and Li, 2014). In karst areas, the entire karst river basin can be divided into a series of small karst sub-basins (Shuster and White, 1971; Birk et al., 2005) to precisely describe the characteristics of the underlying surface of the basin and the corresponding karst development. In addition, the parameters of the distributed model must be calibrated by using historical measured data with physical significance before they can be used to verify the simulation effect, which makes the results of a distributed model more reliable. However, because distributed hydrological models and their parameters are relatively complex (Hartmann et al., 2014, 2015), the greatest challenge of most distributed models used in karst areas is the need for a large amount of hydrogeological data to build the models (Meng et al., 2009; Kraller et al., 2014).

In this study, we improved the physically based and fully distributed Karst-Liuxihe (KL) model (Li et al.,2019a) and developed the improved Karst-Liuxihe (IKL) model to simulate and forecast the effects of urbanization on karst flood events. The improvement was mainly reflected in the runoff generation and confluence algorithms used in the model. The simulation results of karst flood events based on both the KL and IKL models were compared to verify the improvement effects of the KL model. This study focused on the correlation between the built-up land area and flood probability, and the IKL model was used to determine the relationship between the proportion of built-up land area and the flood disaster level in the study area. Four extreme land use scenarios were adopted to quantitatively calculate and assess the influence of
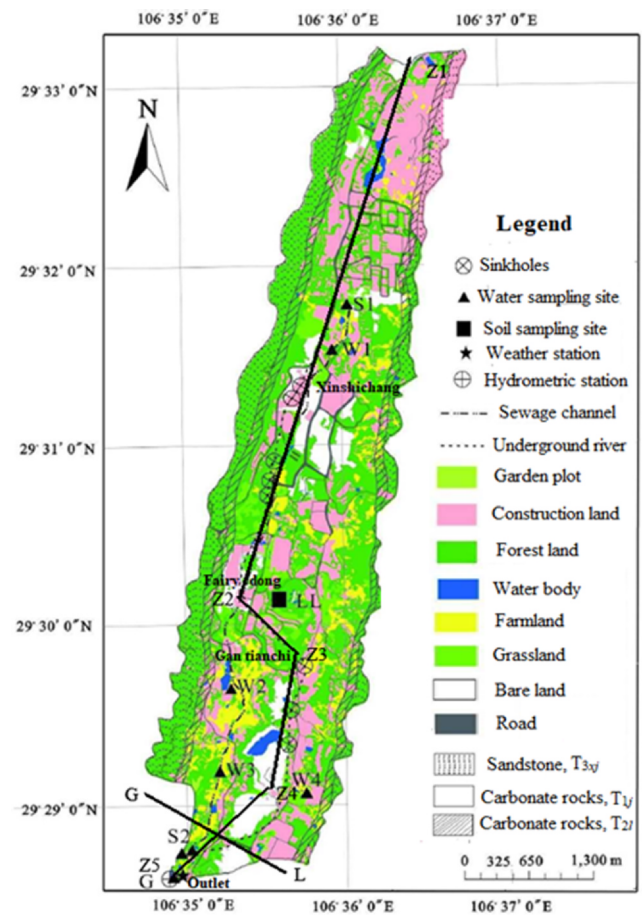

**Fig. 1.** Drainage map of the LKW (modified from Cao, 2012; Zhang, 2017).

urbanization on karst flood events and annual runoff. These extreme scenarios were used to distinguish the contributions of different land use types to annual runoff. The future annual runoff values in 2030, 2040, and 2050 under urban planning were then predicted.

2. Study area and data

The study area in this paper was the Laolongdong karst watershed (LKW) in Chongqing, China. The watershed is located at 106.57–106.61°E and 29.47–29.58°N, and it has a drainage area of 13.1 km^2. The LKW is a developed karst watershed that can effectively represent the entire karst basin of Chongqing. The humid subtropical monsoon climate leads to abundant rainfall in this area, and groundwater recharge mainly comes from precipitation. The multiyear average rainfall was 1080 mm, and the average temperature was 17.8 °C. The bare karst landform in the basin is mainly composed of karst wasteland, some of which has developed into rocky desertification areas. The subsurface karst landform features the extensive development of underground karst caves, crisscrossing karst fissures, water-bearing conduit systems, and the Laolongdong underground river. The drainage map of the LKW is shown in Fig. 1.

2.1. Landform and hydrogeological characteristics

The main landforms of the LKW are low anticline-related hills and intervening valleys. The terrain is high in the north and low in the south, and the average elevation is 500 m. The core of the anticline was subjected to intense karst erosion in the Quaternary, and the inner strata of the basin are mainly carbonate rocks of the lower Triassic Jia Ling Jiang Formation (T$_{1j}$) and have a thickness of approximately
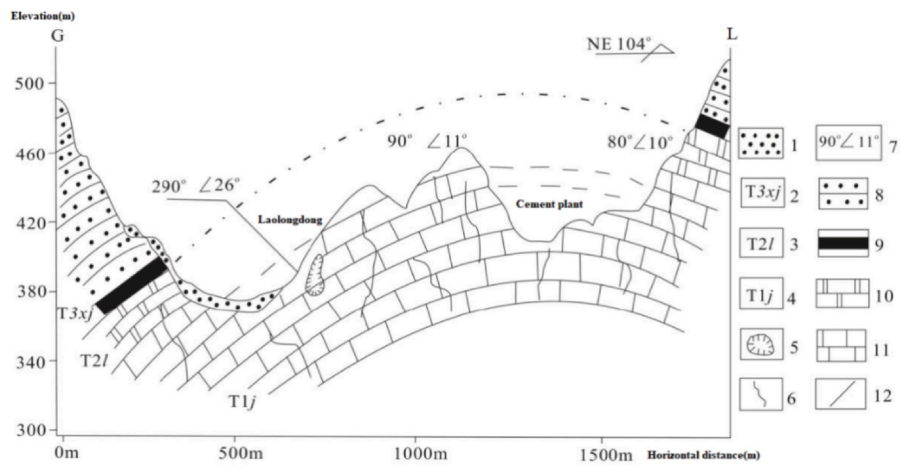
a. Cross-section of the structural map of the catchment outlet: 1=soil layer, 2=T_{3xj}, 3=T_{2l}, 4=T_{1j}, 5=karst cave, 6=karst fissures, 7=orientation of bedrock, 8=sandstone, 9=coal seam, 10=dolomite, 11=limestone, and 12=strata boundary (modified from Cao, 2012).
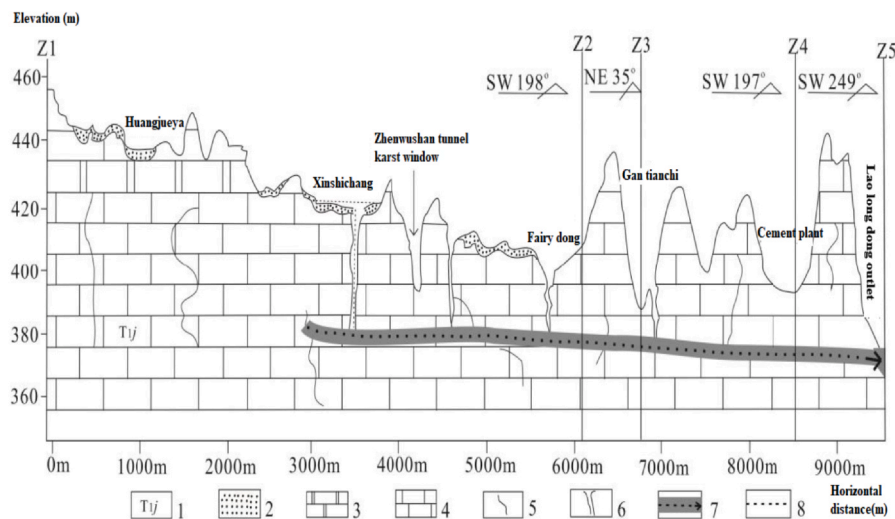
b. Longitudinal section of the structural map: 1=T_{1j}, 2=soil layer, 3=dolomite, 4=limestone, 5=fissures, 6=sinkholes, 7=underground river, 8=sewage channel (modified from Zhang, 2017).

Fig. 2. Structural map of the LKW.

500–700 m. The anticlinal flanks are composed of carbonate rocks of the middle Triassic Lei Kou Po Formation (T_{2l}) and sandstone of the Upper Triassic Xu Jia He Formation (T_{3xj}). Quaternary sediments are distributed sporadically in depressions and on mountainsides. The cross-section of the underground river outlet and a longitudinal section of the structural map of the LKW are shown in Fig. 2.

The anticlinal carbonate rocks are zonally distributed, the slope of the strata in the core of the anticline is gentle, and longitudinal fractures and rock fragmentation create favourable conditions for the development of karst groundwater systems. A large fault zone has developed in the axis of the anticline, and the core of the anticline has developed into a karst aquifer. The sandstones distributed zonally in the eastern and western wings of the anticline form a relative aquiclude. Together, these units constitute a closed and complete underground river system, i.e., the Laolongdong karst underground river, which has a length of 6 km. The river base flow, which is the amount of water in the river channel below the water table, is approximately 50–80 L s^{-1}. Many vertical shafts and sinkholes are distributed in the core of the

anticline in a beaded pattern. Flows on the surface that form after precipitation quickly enter the underground river through the sinkholes; thus, there are no surface rivers in the basin. To better explore the characteristics of the underground river in the study area, a total of 3 tracer tests (Lan, 2014) demonstrated that there was a good hydraulic connection between the sinkholes and the underground river in the LKW, and the karst underground river is likely located in a karst aquifer with large conduits and a flow rate of 1.35 m s^{-1}.

2.2. Property data for the basin

The property data for the LKW included high-resolution DEM data, soil and land use type data, and rainfall and flood process data. The original spatial resolutions of the DEM, soil type, and land use data were 90 m × 90 m, and the resolution was resampled to 30 m × 30 m to perform a detailed simulation of the effect of urbanization on karst flood events using the IKL model. These 3 types of property data were downloaded from the Internet at no cost. The DEM data were from
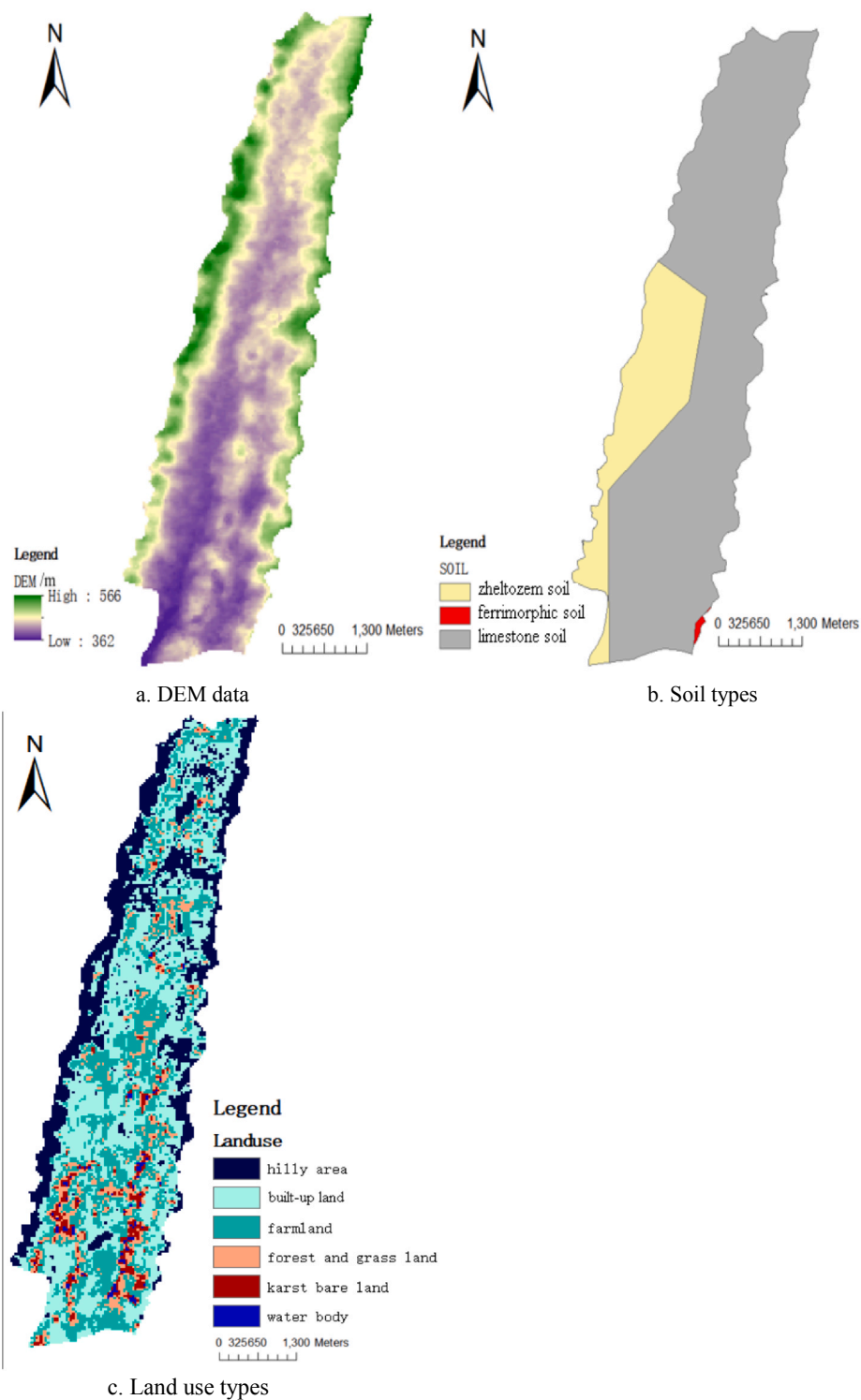
a. DEM data

b. Soil types

c. Land use types

Fig. 3. DEM, soil types, and land use types in the LKW.

http://srtm.csi.cgiar.org, which was last accessed on 02 April 2019. The land use data were from http://landcover.usgs.gov, which was last accessed on 02 April 2019. The soil types were from http://www.isric.org, which was last accessed on 05 April 2019. Fig. 3 shows the DEM, soil types and land use in the LKW.

There are 3 soil types in the study area: zheltozem soil, ferrimorphic soil, and limestone soil. The vegetation is mainly subtropical evergreen broad-leaved forest, and the landforms are dominated by low hills and valleys with steep slopes. Furthermore, the area of sloping cultivated land is 191.8 ha, accounting for 80.0% of the cultivated land area. Bare land is associated with abandoned stone quarries, which are mainly distributed in the middle and southern parts of the basin and account for 7.66% of the total area. Forest and grassland are the main ecological land types in this area, and they are mainly distributed in the sandstone areas on the eastern and western wings of the anticline, accounting for 15.2% and 4.18% of the total area, respectively. The annual runoff processes in the LKW are shown in Fig. 4.
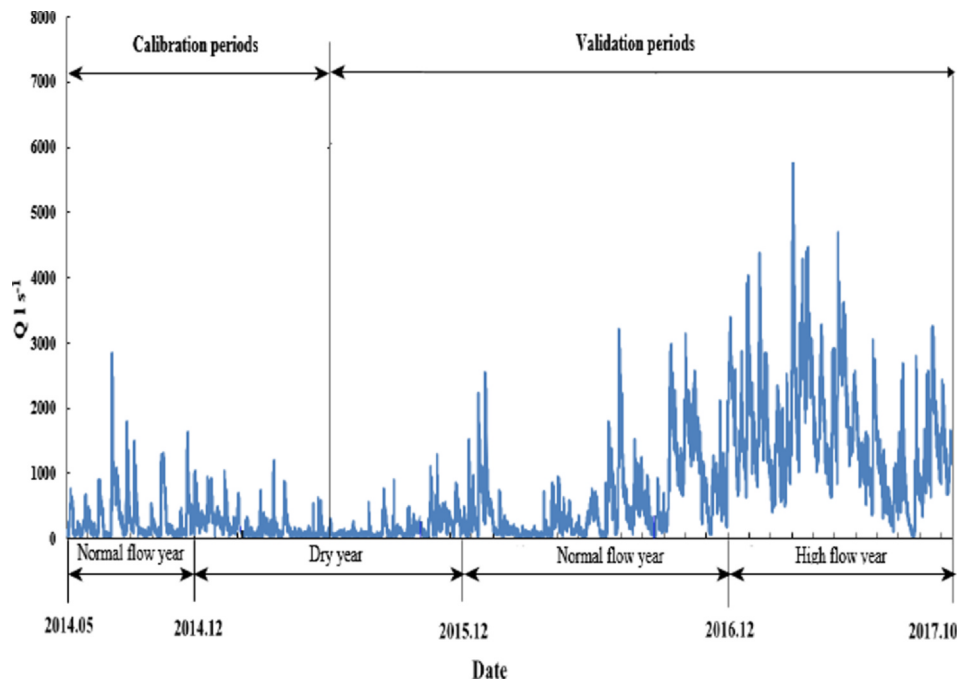
Fig. 4. Annual runoff processes from 2014 to 2017 in the LKW.

2.3. Land use/land cover change during urbanization

In recent years, the research area has undergone rapid urbanization and drastic changes in land use/land cover patterns. In this paper, the specific changes in land use patterns were examined in three stages of urbanization (2005, 2009 and 2019) in the LKW, as shown in Table. 1.

A factor, the proportion of urbanization, was proposed to guide reasonable urbanization development planning in the LKW. This factor represents the ratio of the area of built-up land to the total area of the river basin. According to statistics, there were 105,000 permanent residents in the LKW in 2019, and the urbanization percentage was 99%, which indicates that urbanization had reached a saturation point in the LKW. Additionally, the area of built-up land accounted for 70.2% (Table. 1) of the total basin, which means that the urbanization factor was 70.2% in 2019.

To study the hydrological effect of urbanization in a karst area, this paper proposed 4 extreme scenarios of land use patterns that have occurred or partially occurred in the study area. In scenario 1, the whole

basin is covered by bare karst wasteland without any urbanization or vegetation, and the exposed karst area further evolves into a rocky desertification area in this situation. In scenario 2, the whole area is covered with vegetation. Scenario 3 is the current actual land use situation in the study area. At this time, the urbanization level of the study area has become saturated. In scenario 4, reasonable urbanization development and land use planning are considered. Finally, scenario 0 focuses on the critical land use types of urbanization and is used as the control group. When the proportion of urbanization exceeds the critical value for a given land use type in scenario 0, the underground river entrance exceeds the threshold discharge capacity, and waterlogging occurs as a result. By comparing the simulated runoff values under these 4 extreme land use scenarios, the hydrological effects of different land use patterns were simulated. The 4 extreme scenarios for the land use data in the LKW are shown in Fig. 5.

Table 1
Specific changes in land use patterns in the LKW.

Land use type		2005		2009		2019	
		Area/hm^2	Proportion/%	Area/hm^2	Proportion/%	Area/hm^2	Proportion/%
Agricultural land	farmland	2136	16.3	920	7.0	576	4.4
	garden	569	4.3	689	5.3	654	5.0
	forest	3249	24.8	2948	22.5	1480	11.3
	others	1069	8.2	367	2.8	326	2.5
	total	7024	53.6	4923	37.6	3039	23.2
City and Countryside	city	2291	17.5	4091	31.2	6655	50.8
	countryside	1455	11.1	1076	8.2	373	2.8
	mining	1125	8.6	2036	15.5	2170	16.6
	total	4871	37.2	7203	55.0	9196	70.2
roads		527	4.0	580	4.4	663	5.1
ports		123	0.9	63	0.5	23	0.2
water projects		188	1.4	28	0.2	22	0.2
total		838	6.4	671	5.1	708	5.4
Others	scenic area	246	1.9	205	1.6	106	0.8
	backup land	121	0.9	98	0.7	56	0.4
	total	367	2.8	303	2.3	162	1.2

a. Scenario 0: Critical land use type

b. Scenario 1: The whole basin is covered by bare karst wasteland

c. Scenario 2: The whole area is covered with vegetation.

d. Scenario 3: The current actual land use types

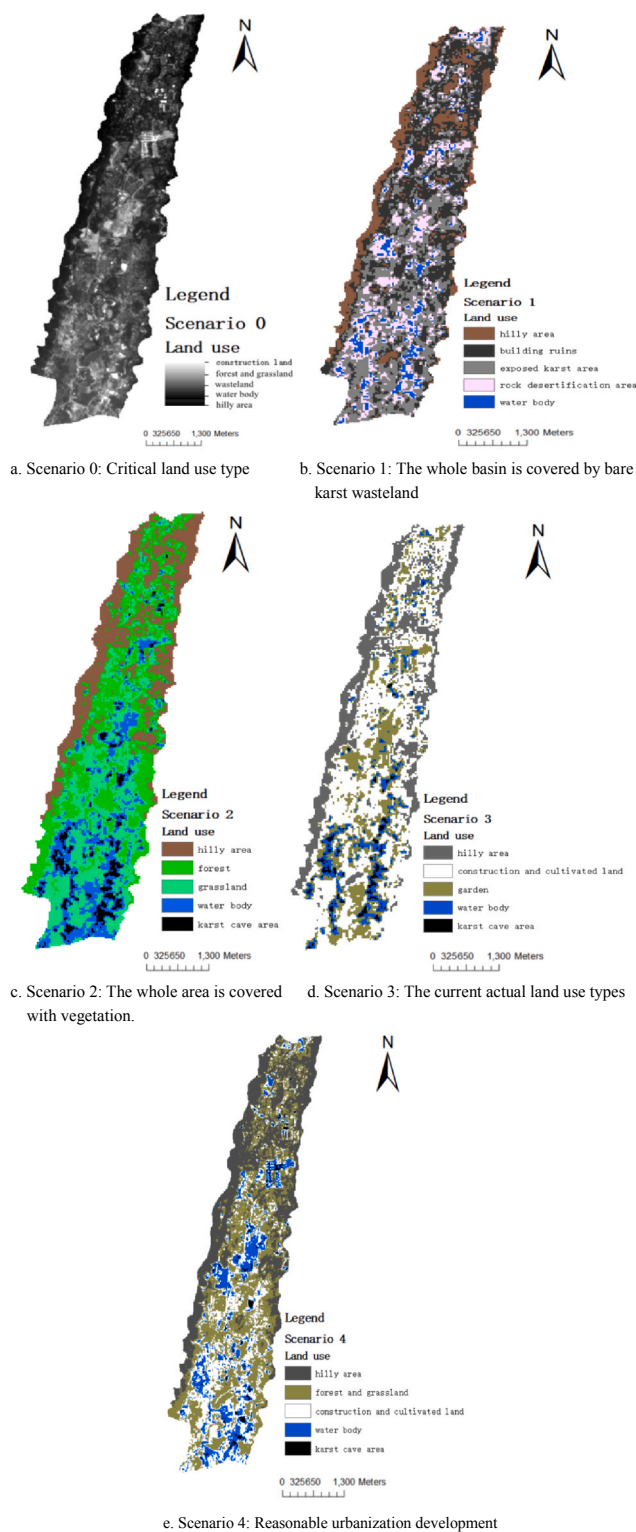e. Scenario 4: Reasonable urbanization development

Fig. 5. Land use data for the 4 extreme scenarios in the LKW.

3. Hydrological model

3.1. Improved Karst-Liuxihe model

The KL model was developed on the basis of the Liuxihe model, which was proposed by Chen Yangbo (2009) of Sun Yat-sen University, China. The Liuxihe model is a terrestrial physically based distributed model that is suitable for surface river simulations and predictions, and

it has achieved good research results (Chen, 2009, 2018; Fan et al., 2012; Li et al., 2017). To overcome the shortcomings of the application of the Liuxihe model in karst areas, a KL model was proposed by Li et al. (2019a) to improve the structure of the original Liuxihe model. However, this KL model uses the same runoff generation and confluence modules to calculate rainfall runoff in karst watersheds, which means that the algorithm for runoff generation and confluence is fixed in this model. Considering that there are many different karst geomorphologic distributions in this study area, with bare karst landforms (Fig. 1) co-existing with buried karst landforms (Fig. 2a), it may not be accurate to use the same algorithm to depict the rain-runoff processes on different geomorphic units, as these predictions would not be consistent with the actual conditions in the basin. To more accurately describe the pattern of runoff concentration under different land use patterns, this study attempted to improve the runoff generation algorithm and confluence modules in the KL model to develop the IKL model, where different rainfall-runoff algorithms were selected for different karst geomorphologic features.

The procedures used to improve the KL model structure were as follows.

1. Improve the generalization methods for karst aquifers in the model

In the KL model, the smallest calculation unit for a karst basin was defined as a karst hydrologic response unit (KHRU) (Li et al., 2019a, b). The KHRU was divided according to the threshold values of the DEM, land use data and soil type data, as well as the interactions of the karst geomorphic media. The specific steps to divide the KHRUs in this study are based on the application of hydrological response units (HRUs) in the SWAT Model by Ren (2006) and the KL model by Li et al. (2019a, b). The water movement and transitions in the KHRU were divided into rapid flow and slow flow based on the width of the karst crack, which was suitable for karst areas under the same land use type. However, the original KL model did not discretize karst aquifers; instead, it divided only the KHRUs and calculated their corresponding hydrological processes. To describe the impact of different land use patterns on the runoff concentration in karst areas based on the IKL model, it was necessary to discretize the karst water-bearing system in the karst aquifers based on the KHRUs.

To facilitate the convergence calculations in the IKL model, the karst aquifers, as the underground structure of the KHRUs, were generalized into a series of small cuboid units according to the properties of karst development. These cuboid units were further divided into L layers, and each layer was divided into M rows and N columns. The location of each cuboid unit was indicated by row number i, column number j, and layer number k. Then, the hydraulic head at the centre of the cuboid unit represented the hydraulic head of the unit, and the permeability boundary was at the edge of the grid cell. The steps to establish the cuboid unit in this study referred to the discrete process for the karst water-bearing system in the CFPM1 module of the MODflow-CFP model (Reimann and Hill, 2009). Fig. 6 shows these cuboid units that represent the simplified karst aquifers.

In the IKL model, a finite difference method (Bittner et al., 2018) was used to calculate the continuous groundwater flows in these cuboid units of the simplified karst aquifers:

$$\begin{cases} \sum_{i=1}^{n} Q_i = \mu^* \Delta h * \Delta V \\ \Delta V = C_j * R_i * L_k \end{cases} \tag{1}$$

where Q_i is the amount of water flowing into or out of the cell per unit time, litres s^{-1} (abbreviated to L s^{-1}, similarly hereinafter); μ is the volumetric specific storage of the karst aquifer, which represents the amount of water absorbed or released per unit volume of an aquifer when the head changes by one unit, L^{-1}; Δh is the change in hydraulic head per unit time m; ΔV is the volume of the valid computational units, m^3; and C_j, R_i, and L_k are the column pitch, row ledge, and layer
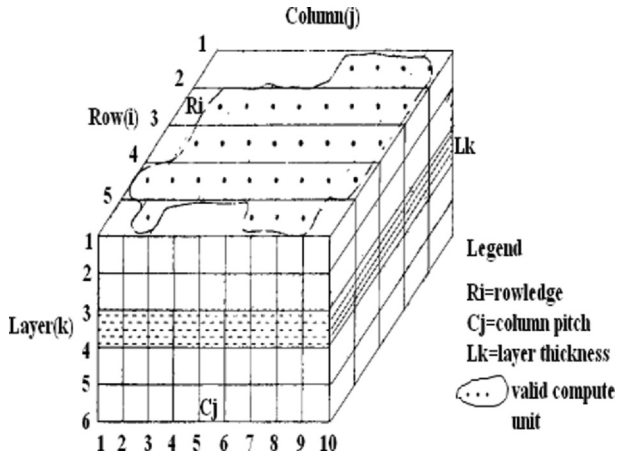
Fig. 6. Spatial dispersion of the karst aquifers.

thickness of the cuboid units (Fig. 6), m, respectively, where i = 1, 2, …, Z; j = 1, 2, …, M; and k = 1, 2, …, N.

In the small cuboid units, the karst aquifer in each unit is heterogeneous, isotropic, and unstable. The calculated hydraulic head value is a function of space and time. Thus, the karst aquifers need to be discretized in space and time. In these cuboid units of the simplified karst aquifer, the valid computational unit (Fig. 6) was regarded as a dual medium that includes a porous medium and a very small fissure, and a partial differential equation was used to describe the hydraulic head values (Beven and Fisher, 1996; Zhang et al.,2009):

$$
\begin{cases}
\frac{\partial}{\partial x}\left[K_s(h-D)\frac{\partial h}{\partial x}\right] + \frac{\partial}{\partial y}\left[K_s(h-D)\frac{\partial h}{\partial y}\right] + \varepsilon_1(x,y,t) - \varepsilon_2(x,y,t) \\
\quad = \mu^*\frac{\partial h}{\partial t} \quad (x,y)\in Z,\ t\geqslant 0 \\
\quad\quad K_s(h-D)\frac{\partial h}{\partial n}\big|_{S_2} = q(x,y,t) \quad (x,y)\in S_2,\ t\geqslant 0 \\
\quad\quad\quad h(x,y,0) = h_0(x,j)y \quad (x,y)\in Z \\
\quad\quad\quad h(x,y,t)\big|_{S_1} = h(x,y,t) \quad (x,y)\in S_1,\ t\geqslant 0
\end{cases}
\tag{2}
$$

where K_s is the permeability coefficient of the karst aquifer, m d⁻¹; h and D are the water level of the aquifer and the elevation of the bottom plate, respectively, m; ε_1 and ε_2 are the infiltration recharge strength and the discharge rate of the aquifer, respectively, m d⁻¹; μ^* is the specific yield in phreatic aquifer, L⁻¹; S_1 and S_2 are aquifer boundaries with type I/Dirichlet conditions (Glass and Guerrero, 2010) and type II/Neumann conditions (Neuman and Elizabeth, 1984); n is the outer normal of S_2; $q(i,j,t)$ is the discharge per unit width of S_2, L³ d⁻¹; $h_0(i,j)$ is the initial water level of the aquifer, m; and Z is the region of the valid computational units.

2. Calculate evapotranspiration under 4 different land use patterns

In the IKL model, the evapotranspiration can be calculated by the following equation (Chen, 2009):

$$
\begin{cases}
E = \lambda E_p, & \text{if } \theta = \theta_{sat} \\
E = \lambda E_p\frac{\theta}{\theta_{fc}}, & \text{if } \theta < \theta_{sat}
\end{cases}
\tag{3}
$$

where E is the actual evapotranspiration, mm; θ_{fc} is the field capacity; θ_{sat} is the saturated water content; E_p is potential evaporation, mm, which can be calculated from the water surface evaporation rate; and λ is the evaporation coefficient, which reflects the vegetation form. In addition, $\lambda = 1-C$, where C is the runoff coefficient. Notably, $C = R/P$, where R is the runoff depth, mm, and P is the precipitation, mm. The range of C is [0, 1], and the wetter the study area is, the greater the C value; λ and C are dimensionless parameters. In the KL model, the runoff coefficient C does not change with the change in land use modes, while it is different for the 4 extreme scenarios of the land use patterns

in the IKL model. Therefore, the evapotranspiration capacities are also different in the 4 scenarios in this study.

3. Rainfall-runoff calculation in the IKL model

In the IKL model, the rainfall-runoff modes were different in the 4 different extreme scenarios: in scenarios 1 and 3, bare karst wasteland and built-up land accounted for most of the basin, and the rainfall-runoff mode was infiltration-excess runoff. The infiltration-excess runoff condition was not considered and calculated in the KL model. Because the background basin of the KL model is extremely wet and almost no bare karst landform exists, it was assumed that there was no infiltration-excess runoff generation (Li et al., 2019a). Under scenario 1 and scenario 3, i.e., where the underlying surface was mainly occupied by bare karst bedrock or built-up land, the infiltration-excess runoff in the IKL model could be calculated by a simplified equation:

$$
\begin{cases}
R_s = CP \\
R_g = 0
\end{cases}
\tag{4}
$$

where R_s is the surface runoff in period t, mm; C is the runoff coefficient; P is the rainfall, mm; and R_g is the groundwater runoff, with $R_g = 0$ under no infiltration or negligible infiltration conditions for bare karst bedrock and built-up land.

In scenario 2, the whole area was covered with vegetation, and in scenario 4, there was reasonable urbanization development and land use planning. The soil infiltration increased under these 2 scenarios, and the rainfall-runoff mode was runoff under saturated storage conditions, which was the same mode as in the KL model. No surface runoff was generated until the water shortage in the vadose zone was full. After the vadose zone was filled, some of the water spilled over to form surface runoff, while the rest continued to seep down into the soil layer and eventually into the underground river system. The runoff generation under scenarios 2 and 4 could be described using the following equation set (Chen, 2018):

$$
\begin{cases}
R_{sm} = (P_m - f_m),\ P_m \geqslant f \\
R_{sm} = 0,\ P_m < f \\
R_{gm} = R_{0m}\exp(-at^b)
\end{cases}
\tag{5}
$$

where R_{sm} is the surface runoff depth in period t, mm; P_m is the rainfall in period t, mm; f is the maximum infiltration rainfall, in terms of depth, mm; f_m is the actual infiltration at that time, mm; R_{gm} is the groundwater runoff depth in the cuboid unit in period t, mm, the cuboid unit represents the simplified karst aquifers (Fig. 6); R_{0m} is the average groundwater runoff depth in period t = 0, mm; and a and b are constants related to the rate of water infiltration.

There was no subsurface runoff generation under scenarios 1 and 3 because the impermeable area covered the whole basin. Under scenarios 2 and 3, subsurface runoff occurred under saturated storage conditions, and the value of runoff generation could be described by Eq. (5). The confluence was divided into the subsurface flow in the soil layers and the underground river system. When the water storage in the soil layer exceeded the field capacity, the water in the soil leaked into the underground river, whereas when it flowed into the soil layer, the subsurface flow could be calculated by the following equation set (Teutsch and Sauter, 1998):

$$
\begin{cases}
\frac{\partial Q_{lat}}{\partial x} = R - Q_{per} - W\cdot z\cdot\frac{\partial\theta}{\partial t} \\
Q_{lat} = v_{lat}\cdot W\cdot z \\
v_{lat} = K_c\cdot\tan(\alpha),\ \theta > \theta_{fc} \\
v_{lat} = 0,\ \theta \leqslant \theta_{fc}
\end{cases}
\tag{6}
$$

where Q_{lat} is the subsurface flow in the soil layers in the x direction, L s⁻¹; W is the width of the cuboid unit that represents the simplified karst aquifers (Fig. 6), dm; z is the thickness of the soil layers, dm; θ is the soil water storage in period t; R is the runoff recharge in a cuboid

unit during period t, which includes the net rainfall and the subsurface flow into the cuboid unit, $dm^2 s^{-1}$; Q_{per} is the seepage, $dm^2 s^{-1}$; v_{lat} is the flow velocity of the subsurface flow, $dm s^{-1}$; K_c is the current soil hydraulic conductivity, $dm s^{-1}$; α is the slope of the cuboid unit; and θ_{fc} is the field capacity. Bates and Campbell (2001) proposed an empirical equation to calculate the numerical relationship between the current soil hydraulic conductivity (K_c) and the saturated hydraulic conductivity (Ks):

$$\frac{K_c}{K_s} = \left(\frac{\theta}{\theta_{sat}}\right)^{2b+3} \tag{7}$$

where θ_{sat} is the saturated water content, $L s^{-1}$, and b is the soil coefficient.

When the water storage in the soil layer exceeds the field capacity, the water in the soil continues to seep down into the underground river system. The seepage Q_{per} can be described by the following equation:

$$\begin{cases} Q_{per} = v_{per} \cdot W^2 \\ v_{per} = K, \theta > \theta_{fc} \\ v_{per} = 0, \theta \leqslant \theta_{fc} \end{cases} \tag{8}$$

where Q_{per} is the seepage water into the underground layer, $L s^{-1}$; v_{per} is the flow velocity of the seepage, $m s^{-1}$; W is the width of the cuboid unit that represents the simplified karst aquifers, m; K is the permeability coefficient of the karst aquifer, $m s^{-1}$; and the meaning of the remaining parameters have been stated previously.

3.2. Model setup

The model setup in this study mainly refers to some initial conditions set before the model runs, which include 1) pre-processing of rainfall and flood data; 2) division of the KHRUs in the model; and 3) estimation of drainage capacity at the entrance of the underground river.

1) Pre-processing of rainfall and flood data

The area of the LKW is very small at only 13.1 km^2, and the hydrological dynamics of the karst underground river are extremely sensitive to the environmental response. To simulate and predict the response of karst floods to urbanization, the temporal scale of these processes was set to 15 min. This scale represents the time step of the simulation, which is a relatively fine scale for flood simulations. Generally, the time scale of simulated flood processes is 1 h. Measurements for a total of 19 karst flood events (2014–2017) from the hydrometric station at the catchment outlet (Fig. 1) were collected in this study. To further reveal the impacts of land use changes on karst runoff in wet, normal, and dry seasons, the annual runoff values for 2017, 2016, and 2015 were selected as representatives of high flow, normal flow, and dry flow years, respectively. In combination with the actual annual runoff situation in the LKW, it was assumed that in a dry flow year, the annual average flow rate was less than 300 $L s^{-1}$, and the maximum flow rate was less than 1500 $L s^{-1}$, whereas in a high flow year, the annual average flow was greater than 1000 $L s^{-1}$, and the maximum flow was greater than 5000 $L s^{-1}$. A year with flows between these ranges was considered a normal flow year.

2) Division of the KHRUs

The establishment of the initial values in the model was based on the input data, such as the DEM data, soil and land use data and karst flood events. The whole watershed was divided into 14,555 KHRUs with high-resolution DEM data, including 1923 river cells and 12,632 hill slope cells. The KHRU was the smallest calculation unit for the karst basin, and more details about KHRUs can be found in Li et al. (2019a, b).

3) Estimation of drainage capacity at the entrance of the underground river.

Before the model was run, it was necessary to determine whether there was waterlogging in the study area. The necessary conditions for waterlogging were related to whether the karst depressions in the basin could retain floodwaters during a rainstorm and whether the flow to the entrance of the underground river exceeded the flood discharge capacity. In this study, a judgement calculation was needed in simulations of rainfall-runoff events with the IKL model. The specific judgement steps are shown below.

1. Calculation of the maximum discharge capacity at the entrance of the underground river in the research area, Q_{max}:

$$\begin{aligned} Q_{max} = A* v &= \pi*(D/2) \wedge 2*v \\ &\approx 3.14*(3.5/2) \wedge 2*1.35 \\ &= 12.98 \ m^3 s^{-1} \end{aligned} \tag{9}$$

where D is the diameter of the entrance of the Laolongdong cave, and the entrance has a regular shape, such as a circle. D is approximately 3.5 m according to field measurements, and V is the flow rate of the underground river at the outlet of LKW, which was determined from the tracer test and was approximately 1.35 $m s^{-1}$.

2. Simulation of the water inflow at the entrance of the underground river, i.e., Q_{in}, based on the IKL model.
3. Comparison of the values of Q_{max} and Q_{in} to determine whether flood detention occurred.

If $Q_{in} > Q_{max}$, then flood detention occurred, and there was an outflow at the underground river outlet, i.e., $Q_{out} = Q_{max}$. The amount of flood detention exceeding the drainage capacity of the underground river entrance was defined as Q_s; if Q_s greater than 0, then as the amount of Q_s continued to increase, the discharge overflow resulted in flooding of low-lying areas of the basin, leading to waterlogging. Q_s was calculated as follows:

$$Q_s = Q_{s1} + Q_{in} - Q_{max} \tag{10}$$

where Q_s is the amount of flood detention during this period, $m^3 s^{-1}$, and Q_{s1} is the storage of flood water from the preceding time period, $m^3 s^{-1}$; if there is no flood detention, then $Q_{s1} = 0$.

If $Q_{in} \leq Q_{max}$, then

$$\begin{cases} Q_{out} = Q_{in} & Q_{in} \leqslant Q_{max}, Q_{s1} = 0 \\ Q_{out} = Q_{in} + Q_{s1} & Q_{s1} > 0, Q_{in} + Q_{s1} \leqslant Q_{max} \\ Q_{out} = Q_{max} & Q_{in} \leqslant Q_{max}, Q_{s1} > 0, Q_{in} + Q_{s1} > Q_{max} \end{cases} \tag{11}$$

The limit discharge capacity of the underground river entrance was 12.98 $m^3 s^{-1}$ (Eq. (9)). Thus, in the IKL model, the simulated critical peak flow discharge was set to 12.98 $m^3 s^{-1}$. It was assumed that the other simulation conditions remained unchanged; that is, the same rainfall and evapotranspiration conditions, soil type, and DEM data were maintained for each KHRU, the smallest unit of the karst basin. Only land use data changed with the simulated flood processes. After several attempts to simulate the floods, the critical land use result (Fig. 5a) at this critical peak flow of 12.98 $m^3 s^{-1}$ was obtained.

3.3. Model running

In this study, the running model refers to building the IKL model to simulate flood events at the underground river outlet and forecast future runoff. There were large differences in the hydrological processes, including evapotranspiration, infiltration, rainfall-runoff, and confluence, due to the differences in the built-up land area and vegetation coverage area. The IKL model was proposed to simulate flood events under these 4 different land use scenarios, and the procedure was as

follows: 1. importing the data for the 4 extreme land use scenarios into the model and assuming that the DEM and soil type data remained unchanged under these 4 different land use scenarios; 2. calculating the evapotranspiration under the 4 scenarios using Eq. (3); 3. calculating the runoff generation (Eqs. (1), (2) and (4), (5)) and confluence (Eqs. (6)–(8)) in the model with different equations; and 4. inputting the rainfall and flood event data into the model and simulating the floods.

In the IKL model, the future antecedent soil moisture before floods, river base flow, future rainfall data, DEM, soil type and land use data were used to effectively forecast future annual runoff in 2030, 2040, and 2050. First, the average value of the antecedent soil moisture before floods could be calculated through continuous rolling simulations of runoff from 2014 to 2017. Second, the future rainfall values were calculated. The multiyear average rainfall for each KHRU was weighted and spread across the entire watershed using the Thiessen polygon method. Finally, future annual runoff was forecasted: initial conditions, such as river base flow and soil moisture, were set as input data for the model in advance, and then rainfall data, DEM elevation, soil type data and future land use data for a certain year in the future were input into the IKL model to forecast future annual runoff. Among these datasets, the future DEM and soil data change much less than the land use data. Hence, the change in annual runoff with land use was mainly simulated here. Future land use data according to reasonable land use planning could be effectively obtained.

In this study, we roughly forecasted the annual runoff for the years 2030, 2040, and 2050. To reduce the uncertainty of the forecast results, it was ensured that the future annual runoff changed with only the land use data, while the remaining variables remained unchanged. Such a processing method was obviously not sophisticated and accurate enough. However, this method was feasible for studying the influence of only land use change on runoff processes and runoff volume in the study area.

3.4. Model parameter optimization and uncertainty analysis

In the IKL model, an improved particle swarm optimization algorithm (Chen et al., 2016; Li et al., 2019a) was used to optimize the model parameters. Data for a total of 19 flood events from 2014 to 2017 were collected in this study. The beginning of the flood process in 2014 and 2015 was the calibration period, and the remaining floods were used for the validation period (Fig. 4). The first five flood events in the calibration period were used for parameter optimization in the model, and the best flood process simulation was used for the final model parameter optimization, while the remaining floods were adopted to validate the model.

The uncertainty analysis of the parameters of the IKL model mainly involved parameter sensitivity analysis in this study. A multiparameter sensitivity analysis (MPSA) method (Choi et al., 1999; Zhang et al., 2018a, b) was used herein to evaluate the sensitivity of the parameters. This method was developed on the basis of the generalized likelihood uncertainty estimation (GLUE) method (Beven and Binley, 1992). The parametric sensitivity analysis included four steps in this study, namely, the definition of the likelihood function, the determination of the parameter value range and prior distribution, parameter sampling, and parameter sensitivity calculation.

First, the likelihood function was determined. The likelihood function was mainly used to determine the fitting degree between the simulated and measured results. The Nash–Sutcliffe coefficient is a relatively comprehensive evaluation index, and it was chosen as the likelihood function in this paper (Chen, 2018; Li et al., 2019a).

$$C = 1 - \frac{\sum_{i=1}^{n} (Q_i - Q_i')^2}{\sum_{i=1}^{n} (Q_i - \bar{Q})^2} \tag{12}$$

where C is the objective function value of the Nash–Sutcliffe coefficient; Q_i and Q_i' are the observed floods and the simulated values,

respectively, L s^{-1}; $\bar{Q}$ is the average value of the observed floods, L s^{-1}; and n is the number of observation periods, hours.

Second, the initial parameter range was determined to be [0.5,1.5] based on the parameter characteristics. The prior distribution of parameters was assumed to be uniform.

Third, 10,000 groups of parameter sets were sampled by the Monte Carlo method, and finally, the sensitivity of various parameters of the model was evaluated by comparing the difference between the prior distribution and posterior distribution. The posterior distribution refers to the probability distribution of each parameter and was calculated according to the simulation results of the parameter optimization. If the prior distribution of the parameter was significantly different from the posterior distribution, then the parameter had a high uncertainty and was considered a sensitive parameter, while if there was no obvious difference between the two, then the parameter had a low uncertainty and was an insensitive parameter. The posterior distribution of the parameters is calculated as follows:

$$\begin{cases} P_{i,\,j}(C \geq C_{i,j}) = \frac{n}{N+1} \times 100 \\ \sigma_i = \sum_{j=1}^{n} (P_{i,j} - \bar{P_{i,j}})^2 \end{cases} \tag{13}$$

where $P_{i,j}$ is the probability of the posterior distribution for the i-th parameter in the j-th series, n is the number of occurrences of the parameter whose likelihood value was greater than or equal to $X_{i,j}$, N is the 10,000 groups of parameter sets by the Monte Carlo method, σ_i represents the sensitivity index of parameter I, and $\bar{P_{i,j}}$ is the average value of the posterior distribution for the i-th parameter in the j-th series.

4. Results and discussion

4.1. Results of model parameter optimization

The simulation results for the parameter optimization process for each of the five flood processes in 2014 and 2015 are shown in Fig. 7, and the evaluation indices of the simulation results are listed in Table. 2.

From the parameter optimization results in Fig. 7, the five flood process simulation results obtained with the IKL model were much better than those obtained with the KL model; in particular, the simulation of flood peak flows was more accurate when the IKL model was used. For further comparison, the evaluation indices of the simulation results based on the 2 models are listed in Table. 2. These findings indicate that compared with those for the KL model, the 6 indices of the flood simulations with the IKL model were greatly improved. The average values of the Nash–Sutcliffe coefficient, C, the correlation coefficient, R, and the coefficient of the water balance, W, increased by 21%, 21%, and 25%, respectively. The process relative error, P%, the relative error of the peak flood flow, E%, and the peak flow time error, T, decreased by 24%, 33%, and 2 h, respectively. Among these evaluation indices, the peak flood flows simulated by the IKL model showed the greatest improvement.

The flood results of these five simulations showed that the effect was optimal for flood 201407050800. Both the simulated peak flow effect and flood process were optimized. The evaluation indices of the simulated flood events in Table. 2 demonstrate that the evaluation indices of flood 201407050800 were the best among those for all floods. Therefore, flood 201407050800 was adopted for the final model parameter optimization. The remaining flood events from 2015 to 2017, the validation period, were used to validate the model performance.

4.2. Model comparison validation and uncertainty analysis

The flood simulation results based on the KL model and the IKL model were compared to verify the improvement effects of the model.
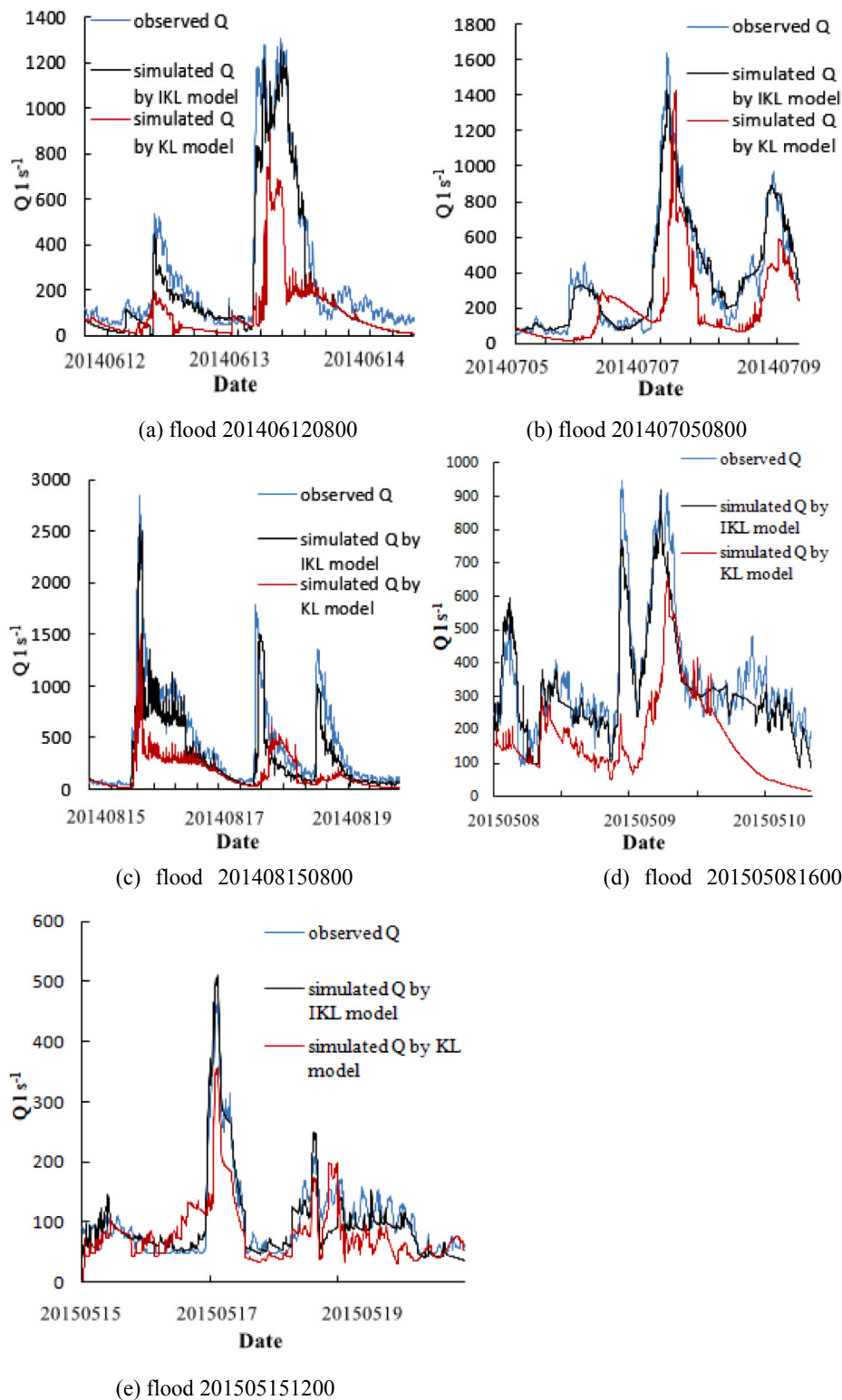
(a) flood 201406120800

(b) flood 201407050800

(c) flood 201408150800

(d) flood 201505081600

(e) flood 201505151200

Fig. 7. Flood process simulation results for parameter optimization.

Data for nineteen flood events were collected from 2014 to 2017; among them, the five floods in the calibration period in 2014 and 2015 were used for parameter optimization. The remaining 14 floods in the validation period from 2015 to 2017 were used for model validation. The simulation effects of the flow processes are shown in Fig. 8.

Fig. 8 shows that the simulated flows based on the KL model were smaller than the observed values. Compared with the simulation results of the KL model, the flood simulation results from 2015 to 2017 were much improved when the IKL model was used. The IKL model results were very satisfactory, especially in terms of simulated peak flows, and the values were very close to the observed values. To further demonstrate the effectiveness of the 2 models, the evaluation indices of these 14 flood simulations were calculated and are listed in Table. 3.

From Table. 3, compared with those for the KL model, the 6 indices of the flood simulations were improved when the IKL model was used. The average values of the Nash–Sutcliffe coefficient, C, correlation

Table 2
Evaluation indices of the simulation results.

Floods	Model	Nash–Sutcliffe coefficient/ C	Correlation coefficient/R	Process relative error/P%	Peak flow relative error/E%	Coefficient of the water balance/W	Peak time error/T (hour)
201406120800	KL	0.67	0.62	45	55	0.67	−7
	IKL	0.85	0.89	16	15	0.92	−5
201407050800	KL	0.65	0.64	34	45	0.72	−6
	IKL	0.92	0.91	12	8	0.95	−3
201408150800	KL	0.61	0.63	48	64	0.52	−5
	IKL	0.88	0.85	14	11	0.93	−4
201505081600	KL	0.75	0.75	34	25	0.74	−5
	IKL	0.91	0.87	14	12	0.93	−2
201505151200	KL	0.72	0.71	29	36	0.76	−4
	IKL	0.90	0.89	16	15	0.94	−2
average value	KL	0.68	0.67	38	45	0.68	−5
	IKL	0.89	0.88	14	12	0.93	−3

coefficient, R, and coefficient of the water balance, W, increased by 23% 23%, and 26%, respectively, while the process relative error, P%, flood peak flow relative error, E%, and peak flood flow time error, T, decreased by 21%, 22%, and 3 h, respectively. These evaluation indices suggest that the IKL model functioned better than the KL model in karst flood simulation.

The runoff generation and confluence algorithm were fixed in the KL model (Li et al., 2019a, b). However, the same runoff calculation method may not be able to accurately describe the complex hydrological processes under different LUCCs in karst areas. In the IKL model, different runoff generation and confluence algorithms were adopted according to the different types of land use. Such a treatment was obviously consistent with the real situation of the study area. Therefore, this IKL model performed better than the KL model in karst flood simulations (Fig. 3 and Table. 8).

To further reflect the impact of land use changes on annual runoff in wet, normal, and dry seasons, the annual runoff values from 2017, 2016, and 2015 were chosen to represent high flow, normal flow, and dry flow years, respectively. The values of the flow process throughout the year simulated by the 2 models from 2014 to 2017 are shown in Fig. 9.

Based on the results shown in Fig. 9, the simulated flow process throughout the year based on the KL model was smaller than the observed values. The simulation results based on the IKL model were very close to the observed values. Compared with the results of the KL model, the flow processes simulated by the IKL model were much improved, and the results were consistent with the flood event simulation results throughout the years (Fig. 8 and Table. 3). Table. 4 shows the evaluation indices of these annual runoff simulations.

Table. 4 shows that the average values of the Nash–Sutcliffe coefficient (C), correlation coefficient (R), process relative error (P%), peak flood flow relative error (E%), coefficient of the water balance (W), and peak flood flow time error (T) based on the KL model were 0.65, 0.65, 34%, 42%, 0.61, and 7 h, respectively, and those based on the IKL model were 0.89, 0.90, 15%, 18%, 0.91, and 4 h, respectively. All indices markedly improved with the new model, which confirmed that the IKL model functioned better than the KL model in the karst flood simulations. Additionally, all the flood process simulation results using the IKL model were satisfactory in wet, normal, and dry seasons, indicating that this model was potentially applicable to all runoff situations. The uncertainty analysis of the parameters for the IKL model mainly involved parameter sensitivity analysis in this study. The computational steps of parameter sensitivity analysis can be found in section 3.3, and the formulas for the calculation of parameter sensitivity are shown in Eqs. (12) and (13). Flood 201407050800, which was selected for parameter optimization, was used to calculate the parameter sensitivity. Table. 5 lists the parameter sensitivity calculation results for the IKL model.

In Table. 5, the values of σ_i represent the sensitivity of parameter i.

The higher the value of σ_i is, the more sensitive the parameter is. The rainfall infiltration coefficient was the most sensitive parameter in the IKL model, which showed that the amount of rainfall infiltration had the greatest influence on the outlet discharge of the underground river in the study area. This finding was consistent with the main replenishment source of the underground river in the study area being infiltrating rainfall water. The parameter sensitivity sequence of the IKL model was as follows: rainfall infiltration coefficient, θ_p > saturated hydraulic conductivity, K_s > rock porosity, R_p > saturated water content, θ_{sat} > field capacity, θ_{fc} > specific yield S_y > soil coefficient, b > flow direction F_d > thickness of epikarst zone, h > channel roughness, n_l > slope roughness, n > evaporation coefficient, λ > potential evaporation, E_p > depletion coefficient, ω > wilting percentage, C_{wl}. The parameters associated with evaporation, including the evaporation coefficient, potential evaporation, and wilting percentage, were insensitive parameters, which showed that they had little influence on the flood simulation results. This finding was consistent with the small proportion of evapotranspiration during a flood event. The depletion coefficient of underground runoff was an insensitive parameter, which implied that the amount of water in the flood receding stage occupied a small proportion of the total flood amount.

4.3. Flood simulation results for 4 extreme scenarios of land use patterns

In this study, the simulated flow process values under 4 extreme land use scenarios were compared based on the KL and IKL models, and the hydrological effects of different land use patterns associated with urbanization were evaluated in detail. Fig. 10 shows the flow processes simulated by the IKL model under these 4 scenarios in the LKW. Tables. 6 and 7 show the simulated indices and the related statistical parameters (annual runoff, runoff depth and runoff coefficient) under the 4 land use scenarios.

From the simulated flow process results in Fig. 10, Tables. 6 and 7, the simulated results under scenario 4 (reasonable urbanization development) were optimal and closest to the actual observed values. Under scenario 3 (the current actual land use situation), the total amounts of simulated flows were largest, and the simulated peak flood process curves were steepest, which suggests that the increase in the built-up land area associated with urbanization increased the volume of runoff and significantly increased the peak flow. Under scenario 1 (all areas were bare karst wastelands), the simulated flow values were the second largest. The flow process, runoff depth, and runoff coefficient simulated under scenario 3 and scenario 1 were larger than the observed values, which indicated that increasing the built-up land and wasteland areas could increase the total annual runoff and the peak flow. Under scenarios 1 and 3, the land use patterns led to an increase in runoff and potentially to catastrophic flooding in the study area. Under scenario 2 (all areas were vegetated), the simulated flow process
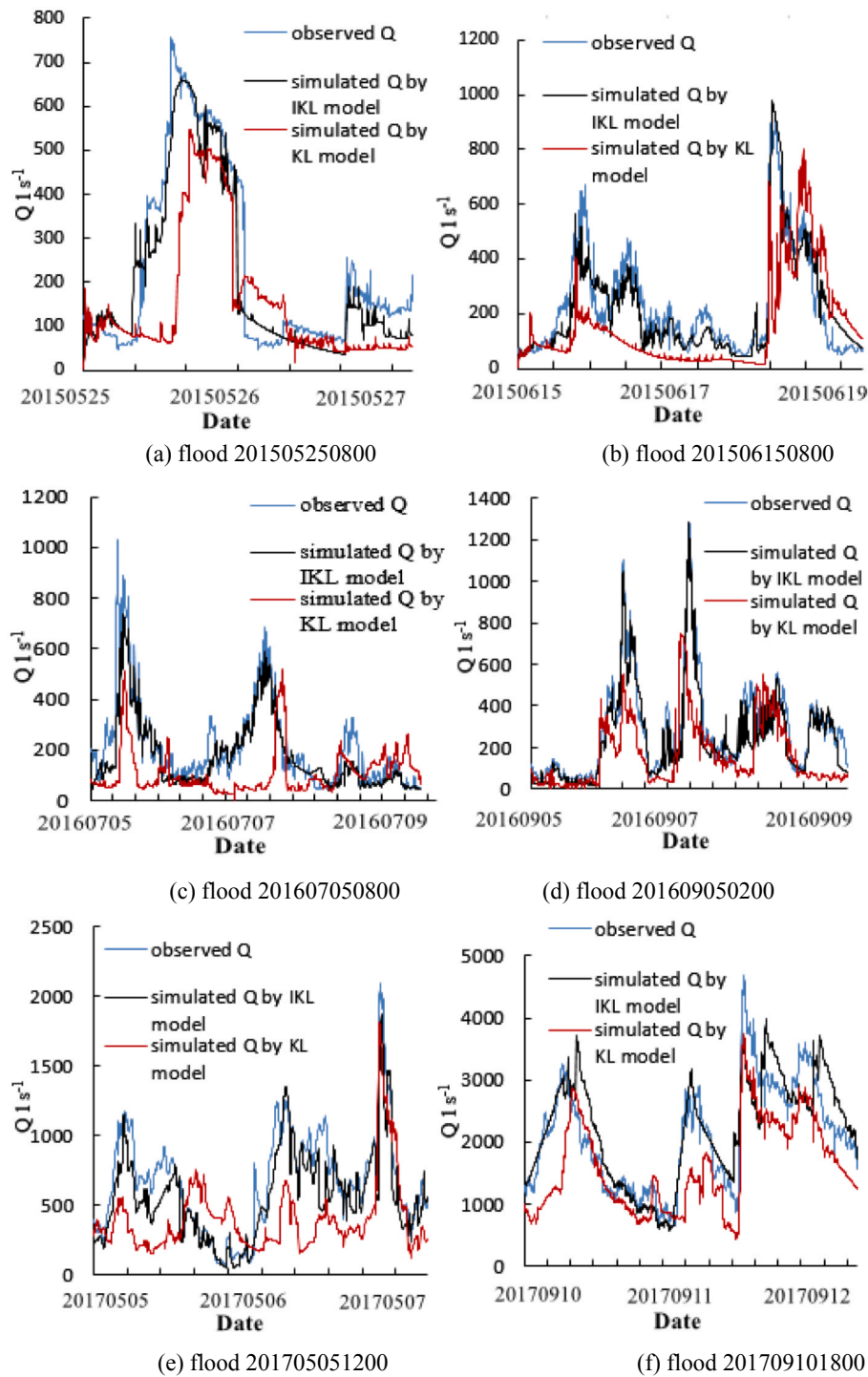
(a) flood 201505250800   (b) flood 201506150800

(c) flood 201607050800   (d) flood 201609050200

(e) flood 201705051200   (f) flood 201709101800

Fig. 8. Flood process simulation results for model validation.

values were the smallest. The simulated flood peak process curves were the most gradual under this scenario (Fig. 10), and the simulated peak flows were smaller than the observed values, which indicated that an increase in vegetation could reduce the volume of runoff.

As shown in Table. 7, the comparison of the simulated flow process values under the 4 land use scenarios indicated that the average value of simulated flows from 2014 to 2017 was 9,079,830 m^3 under land use scenario 1, 7,037,451 m^3 under land use scenario 2, 9,484,703 m^3 under land use scenario 3, and 7,354,684 m^3 under land use scenario 4. Thus, the order of the flow volumes simulated under these 4 extreme land use scenarios was as follows: scenario 3 > scenario 1 > scenario

4 > scenario 2. When these 4 land use modes were converted to one another, the associated hydrological effects of urbanization also changed. The sensitivity order of the urbanization effect on annual runoff was as follows: scenario 2 converted to scenario 3 (9,484,703–7,037,451 = 2,447,252 m^3) > scenario 3 converted to 4 (9,484,703–7,354,684 = 2,130,019 m^3) > scenario 1 converted to 2 (9,079,830–7,037,451 = 2,042,379 m^3).

4.4. Flood forecasting results according to land use pattern planning

The IKL model was used to quantify how the proportion of built-up

Table 3
Evaluation indices of the karst flood simulations for model validation.

Floods	Model	Nash–Sutcliffe coefficient/C	Correlation coefficient/R	Process relative error/P%	Peak flow relative error/E%	Coefficient of water balance/W	Peak time error/T (hour)
201505250800	KL	0.67	0.65	37	42	0.67	8
	IKL	0.83	0.88	22	20	0.89	4
201506150800	KL	0.62	0.61	42	38	0.71	−7
	IKL	0.9	0.85	17	17	0.91	−4
201508200800	KL	0.64	0.69	45	58	0.54	8
	IKL	0.85	0.89	14	19	0.88	5
201605150800	KL	0.73	0.68	38	29	0.65	5
	IKL	0.86	0.92	25	9	0.85	2
201606181800	KL	0.63	0.65	38	28	0.54	−5
	IKL	0.82	0.85	26	11	0.84	−2
201607050800	KL	0.65	0.71	34	38	0.75	5
	IKL	0.92	0.91	11	13	0.92	3
201608151200	KL	0.63	0.66	32	29	0.74	5
	IKL	0.93	0.94	12	14	0.94	3
201609050200	KL	0.62	0.69	39	45	0.67	−4
	IKL	0.88	0.89	17	22	0.85	−3
201705051200	KL	0.63	0.64	42	29	0.52	−5
	IKL	0.89	0.86	18	17	0.88	−2
201705210200	KL	0.63	0.66	45	34	0.67	6
	IKL	0.87	0.88	17	15	0.91	3
201706180800	KL	0.67	0.64	33	42	0.59	−7
	IKL	0.85	0.87	15	12	0.95	−4
201707101200	KL	0.61	0.63	38	35	0.73	−6
	IKL	0.9	0.91	16	9	0.93	−3
201708051200	KL	0.62	0.64	35	28	0.64	6
	IKL	0.91	0.88	17	15	0.91	3
201709101800	KL	0.63	0.65	40	42	0.72	7
	IKL	0.85	0.86	21	23	1.05	5
average value	KL	0.65	0.66	38	37	0.65	6
	IKL	0.88	0.89	17	15	0.91	3

land area was related to flooding in the study area. The critical land use data could be identified by setting the underground river drainage capacity (12.98 m^3 s^{-1} in Eq. (9)) in the model. The critical land use data are shown in Fig. 5a (scenario 0). In scenario 0, the statistical results showed that the built-up land area accounted for 45% of the total basin area, which means that the urbanization proportion factor was 45%. When this proportion exceeded 45%, the amount of water at the underground river entrance exceeded the limit discharge capacity of 12.98 m^3 s^{-1}, and waterlogging could occur in the study area.

Section 2.3 indicates that urbanization reached a saturation point in 2019, and the urbanization proportion factor was 70.2%. According to the urbanization development requirements of the local government, the optimal urbanization proportion factor is 30%, and this level must be achieved by 2050. Therefore, we determined that the urbanization proportion factor must decrease by 1.26% per year. Thus, reasonable urbanization development could be achieved in this way, as shown in Table. 8.

The future annual runoff (2030, 2040, and 2050) could be forecasted according to rational land use pattern planning. The steps in annual runoff forecasting are shown in section 3.2. The forecasting results are shown in Table. 9.

In Table. 9, the annual runoff in 2019 was simulated based on the IKL model for comparison with future annual runoff forecasting results. Notably, the annual runoff will decrease each year. In 2019, the simulated annual runoff was largest at 10,224,655 m^3, and it was projected to reach 5,548,620 m^3 in 2050. Thus, under the optimal urbanization development scheme for the LKW, runoff in 2050 will decrease by 4,676,035 m^3 compared to the current value, a decline of 45.7%. The runoff depth and the runoff coefficient were projected to decrease by 46% and 48%, respectively. Thus, after 30 years of reasonable urbanization, the annual runoff reduction will be obvious. The forecasted annual runoff results for 2030, 2040, and 2050 can provide the necessary theoretical basis for local flood control decision making in the future.

The study area, i.e., the Laolongdong karst watershed in Southwest China, has been a experienced rapid urbanization in recent years. The constructionThe area of built-up land is increasing year by year-annually, crowding outreplacing the original ecological green space to an increasingly large extent (Cao, 2012). The increase ofin built-up land construction area leads has led to thean increase ofin the impermeable area and thea decrease ofin infiltration in the basin, and the final result is the frequent occurrence of catastrophic floods (Zhang, 2017). For instance, Fairy Dong (Fig. 1), once a famous tourist attraction, was closed after a waterlogging incident. Therefore, it is necessary to build a model to quantitatively analyseanalyze the correlation between urbanizedation area and catastrophic flooding, and an improved model (IKL) was developd in this study to simulate and forecast the hydrological effects of urbanization in the study area. The results of flood simulation based on this IKL model were reasonable and satisfactory, indicating that the improvement of the KL model was effective and this imorved IKL model was applicable to the simulation and forecasting of the effects of urbanization on flood events in karst basins.

5. Conclusions

The structure and parameters of commonly used distributed hydrological models are relatively complex (Hartmann et al., 2014, 2015; Kraller et al., 2014) and require considerable hydrogeological data when building models of karst areas (Meng et al., 2009). To overcome the problem of high modelling cost in karst hydrological simulation, this study attempted to improve the structure and algorithm of the KL model (Li et al., 2019a, b) and developed the IKL model to simulate and forecast the effects of urbanization on karst floods. This IKL model exhibits excellent application potential in karst areas due to its relatively simple structural characteristics; for instance, in terms of vertical structure, there are only two underground layers. Consequently, it requires less data for modelling than other hydrological models. In addition, the IKL model has fewer parameters than other distributed
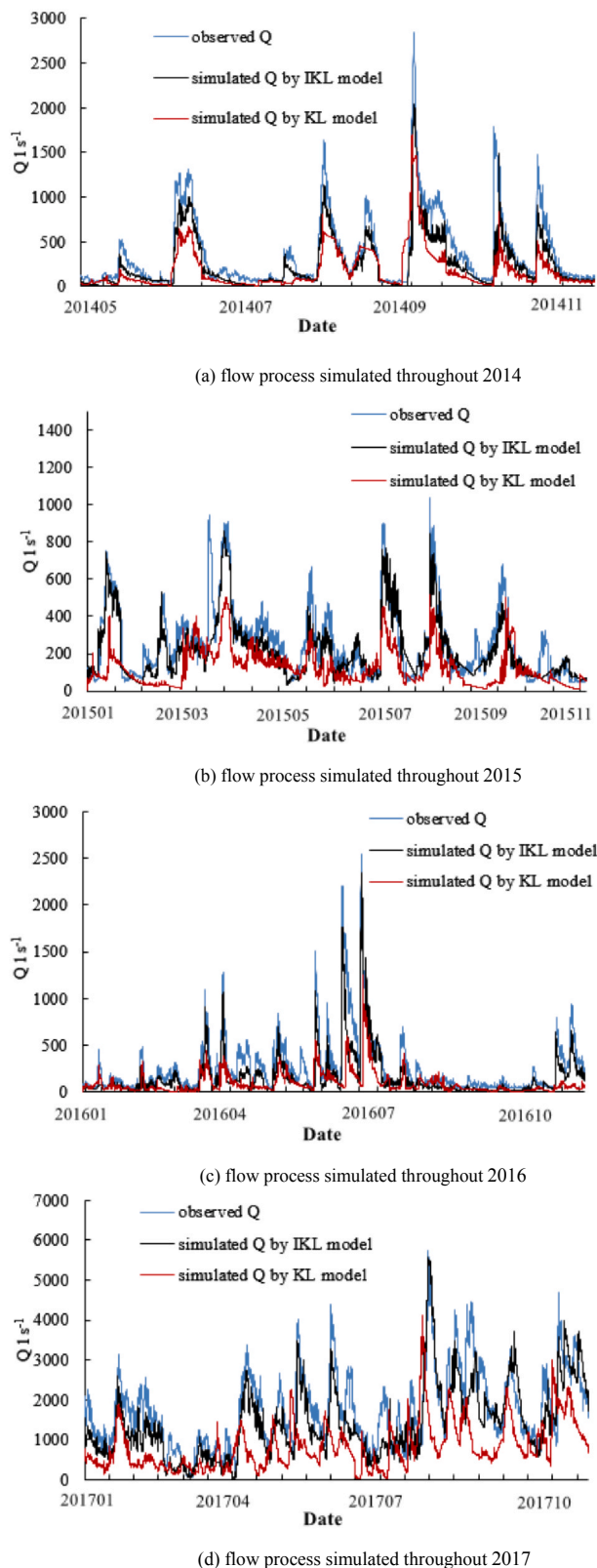
(a) flow process simulated throughout 2014

(b) flow process simulated throughout 2015

(c) flow process simulated throughout 2016

(d) flow process simulated throughout 2017

Fig. 9. Simulated flow processes in different years based on the 2 models.

models (Li et al., 2019a), which makes it relatively easy to construct models of karst areas. Finally, the karst flood simulation and forecast results were quite good, which indicated the applicability of the model to karst basins. The following conclusions were obtained based on the research results in this study.

1. Nineteen flood events from 2014 to 2017 were used to test the performance of the IKL and KL models. The karst flood simulation results from the IKL model were much better than those from the KL model; in particular, the simulated peak flows were very close to the observed values. Compared with those for the flood results simulated by the KL model, the evaluation indices of the karst flood simulations based on the IKL model showed considerable improvement: the average values of the Nash–Sutcliffe coefficient, C, correlation coefficient, R, and coefficient of the water balance, W, increased by 23%, 23%, and 26%, respectively, and the process relative error, P%, flood peak flow relative error, E%, and flood peak flow time error, T, decreased by 21%, 22%, and 3 h, respectively.

2. The annual runoff values from 2017, 2016, and 2015 were selected to represent the values of a high flow year, normal flow year, and dry flow year, respectively. The simulated annual runoff values from 2014 to 2017 were close to the observed values. The average values of the 6 evaluation indices were 0.89, 0.90, 0.15, 0.18, 0.91, and 4 h, which implied that all the flood simulation results from the IKL model in the wet, normal and dry seasons were satisfactory.

3. The parameter sensitivity analysis of the IKL model showed that the rainfall infiltration coefficient was the most sensitive parameter in the IKL model, while the wilting percentage was the least sensitive parameter. The parameter sensitivity sequence of the IKL model was as follows: rainfall infiltration coefficient > saturated hydraulic conductivity > rock porosity > saturated water content > field capacity > specific yield > soil coefficient > flow direction > thickness of epikarst zone > channel roughness > slope roughness > evaporation coefficient > potential evaporation > depletion coefficient > wilting percentage.

4. The IKL model was proposed in this study to provide detailed simulations of 4 extreme scenarios with different land use patterns of urbanization. The simulated results indicated that the increase in the built-up land area increased the volume of runoff more than any other factor, such as the peak flow and bare karst wasteland area, which had the second- and third-largest effects, respectively. However, the increase in vegetation could reduce the volume of runoff. The annual runoff volume simulated under these 4 extreme land use scenarios displayed the following order: scenario 3 > scenario 1 > scenario 4 > scenario 2. The order of the effects of urbanization on annual runoff was as follows: scenario 2 converted to scenario 3 > scenario 3 converted to scenario 4 > scenario 1 converted to scenario 2.

5. In 2019, the urbanization of the LKW reached a saturation point, and the urbanization proportion factor was 70.2%. The optimal proportion factor was 30%, and the critical proportion factor was 45%. When the proportion factor exceeded 45%, waterlogging could occur in the LKW. Compared with the simulated annual runoff value in 2019, the forecasted annual runoff value in 2050 decreased by 45.7%, and the reduction was obvious after 30 years of reasonable urbanization. Future annual runoff forecasting results can provide the necessary theoretical basis for decision making related to local flood control.

6. Data availability**a

All data used in this paper are available, findable, accessible, interoperable, and reusable (FAIR).

The rainfall data and karst flood events were observed at field observation stations in the LKW. The watershed property data, including high-precision DEM data, land use data and soil type data, can be downloaded from the Internet at no cost. The DEM data were from http://srtm.csi.cgiar.org, which was last accessed on 02 April 2019. The land use data were from http://landcover.usgs.gov, which was last accessed on 02 April 2019. The soil type data were from http://www.isric.org, which was last accessed on 05 April 2019. The prototype of the Liuxihe model was provided by Yangbo Chen, Sun Yat-sen

Table 4
Evaluation indices of the annual runoff simulations from 2014 to 2017.

Annual runoff	Model	Nash–Sutcliffe coefficient/C	Correlation coefficient/R	Process relative error/P%	Peak flow relative error/E%	Coefficient of water balance/W	Peak time error/T (hour)
2014	KL	0.63	0.65	34	46	0.62	−7
	IKL	0.89	0.92	12	21	0.93	−3
2015	KL	0.65	0.68	34	42	0.64	−6
	IKL	0.91	0.93	14	18	0.92	−4
2016	KL	0.67	0.64	32	41	0.56	7
	IKL	0.87	0.89	18	19	0.89	5
2017	KL	0.63	0.62	35	40	0.61	6
	IKL	0.88	0.87	17	15	0.91	3
average value	KL	0.65	0.65	34	42	0.61	7
	IKL	0.89	0.9	15	18	0.91	4

Table 5
The parameter sensitivity results in the IKL model.

Floods	Infiltration coefficient/θ_p	Potential evaporation/E_p	Evaporation coefficient/λ	Wilting coefficient/C_{wl}	Thickness of epikarst zone/h
201407050800	0.91	0.36	0.41	0.20	0.65
	Soil coefficient/b	Saturated water content/θsat	Rock porosity/R_p	Field capacity/θfc	Permeability coefficient/K_s
	0.78	0.85	0.86	0.82	0.88
	Flow direction/F_d	Slope roughness/n	Depletion coefficient/ω	Specific yield/S_y	Channel roughness/n_1
	0.74	0.62	0.33	0.80	0.64

(a) flow process simulated throughout 2014 under the 4 scenarios

(c) flow process simulated throughout 2016 under the 4 scenarios

(b) flow process simulated throughout 2015 under the 4 scenarios

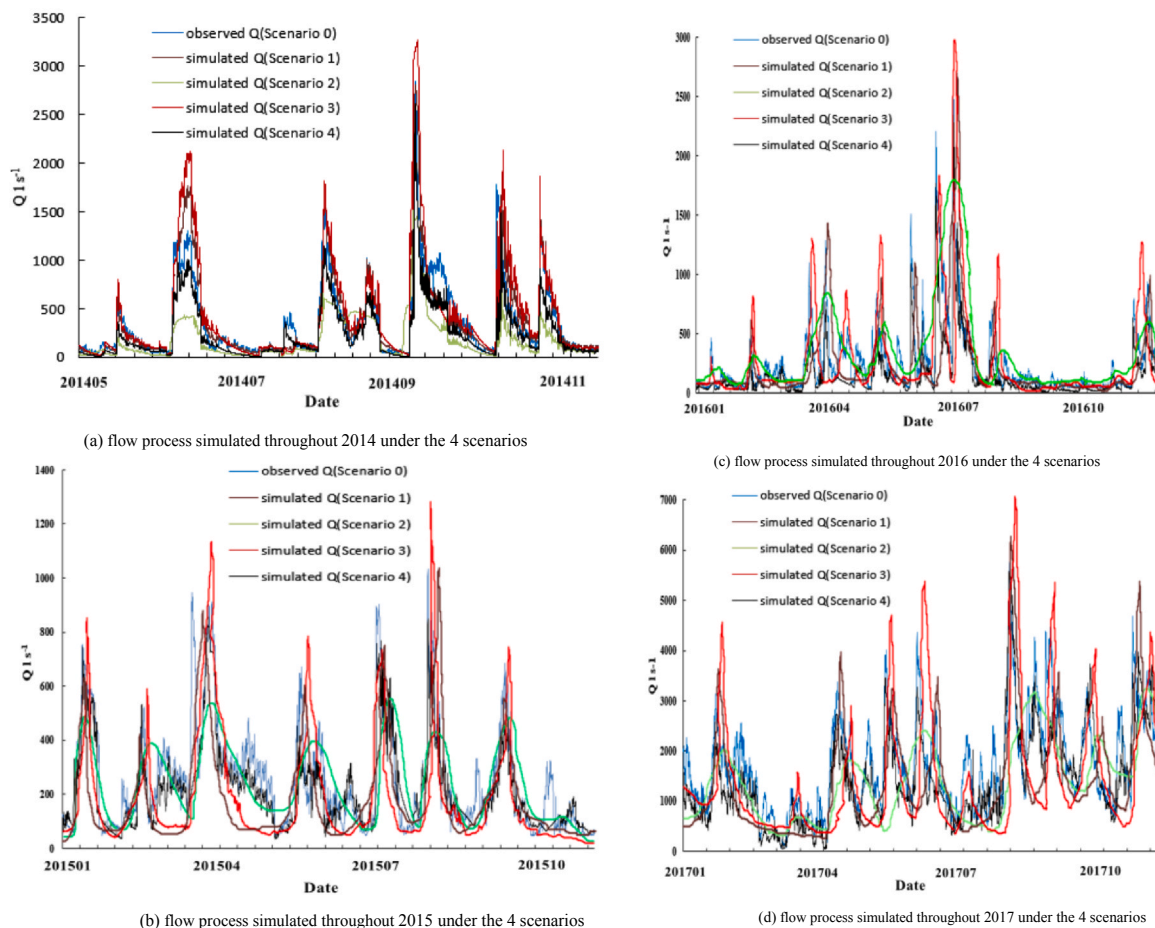(d) flow process simulated throughout 2017 under the 4 scenarios

Fig. 10. Simulated flow processes under the 4 extreme land use scenarios in the LKW.

University, Guangzhou, China.

7. Author contributions**a

Table 6
Evaluation indices of annual runoff under the 4 land use scenarios.

Scenario	Annual runoff	Nash–Sutcliffe coefficient/C	Correlation coefficient/R	Process relative error/P%	Peak flow relative error/E %	Coefficient of water balance/W	Peak time error/T (hour)
Scenario 1: All bare karst wasteland	2014	0.83	0.82	0.21	0.2	1.18	4
	2015	0.81	0.84	0.23	0.21	1.25	5
	2016	0.82	0.83	0.18	0.17	1.12	−3
	2017	0.85	0.85	0.2	0.19	1.18	5
Scenario 2: All vegetation	2014	0.78	0.8	0.35	0.48	0.38	−5
	2015	0.75	0.78	0.32	0.35	0.55	4
	2016	0.8	0.75	0.28	0.32	0.62	−5
	2017	0.77	0.79	0.31	0.45	0.54	5
Scenario 3: The current actual land use situation	2014	0.82	0.83	0.23	0.22	1.25	5
	2015	0.8	0.85	0.25	0.26	1.32	6
	2016	0.81	0.8	0.21	0.23	1.18	−4
	2017	0.86	0.83	0.22	0.25	1.27	7
Scenario 4: Reasonable urbanization development	2014	0.89	0.91	0.18	0.12	0.95	3
	2015	0.88	0.89	0.16	0.15	0.92	4
	2016	0.91	0.92	0.13	0.11	0.89	−3
	2017	0.92	0.93	0.15	0.17	0.88	−5

Table 7
Statistical parameters for simulated annual runoff.

Scenario	Time	Observed annual runoff, m³	Simulated annual runoff, m³	Observed runoff depth, m	Simulated runoff depth, m	Observed runoff coefficient	Simulated runoff coefficient	Relative error, %
Scenario 1: All bare karst wasteland	2014	7,491,377	8,598,452	0.57	0.66	0.53	0.61	15
	2015	4,345,818	4,905,645	0.33	0.37	0.31	0.35	13
	2016	8,237,654	9,525,479	0.63	0.73	0.58	0.67	16
	2017	10,805,705	13,289,745	0.82	1.01	0.76	0.94	23
Scenario 2: All vegetation	2014	7,491,377	6,758,650	0.57	0.52	0.53	0.48	−10
	2015	4,345,818	3,875,687	0.33	0.3	0.31	0.27	−11
	2016	8,237,654	7,458,623	0.63	0.57	0.58	0.53	−9
	2017	10,805,705	10,056,842	0.82	0.77	0.76	0.71	−7
Scenario 3: The current actual land use situation	2014	7,491,377	8,956,250	0.57	0.68	0.53	0.63	20
	2015	4,345,818	5,245,850	0.33	0.4	0.31	0.37	21
	2016	8,237,654	9,878,650	0.63	0.75	0.58	0.7	20
	2017	10,805,705	13,858,060	0.82	1.06	0.76	0.98	28
Scenario 4: Reasonable urbanization development	2014	7,491,377	7,050,460	0.57	0.54	0.53	0.5	−6
	2015	4,345,818	4,056,800	0.33	0.31	0.31	0.29	−7
	2016	8,237,654	7,905,250	0.63	0.6	0.58	0.56	−4
	2017	10,805,705	10,406,224	0.82	0.79	0.76	0.74	−4

Table 8
Future reasonable land use planning in the LKW.

Land use type	2019		2030		2040		2050	
	Area/hm²	Proportion/%	Area/hm²	Proportion/%	Area/hm²	Proportion/%	Area/hm²	Proportion/%
Agricultural land	1229.4	9.4	1613.9	12.3	2360.6	18	2999.9	22.9
Construction land	9202	70.2	7755.2	59.2	5488.9	41.9	3930	30
Water body	352.5	2.7	772.9	5.9	1304.8	10	1572	12
Forest and grass	2308.8	17.6	2947.5	22.5	3930	30	4585	35
Other land use type	7.2	0.1	10.49	0.1	15.7	0.1	13.13	0.1

Table 9
Forecasted future annual runoff results according to the land use pattern.

Time	Runoff, m³	Runoff depth, m	Runoff coefficient
2019	10,224,655	0.78	0.75
2030	8,525,650	0.69	0.65
2040	6,845,600	0.56	0.48
2050	5,548,620	0.42	0.39

References

Ambroise, B., Beven, K., Freer, J., 1996. Toward a generalization of the TOPMODEL concepts: Topographic indices of hydrologic similarity. Water Resour. Res. 32, 2135–2145.

Bates, B.C., Campbell, E.P., 2001.A.A. Markov chain Monte Carlo scheme for parameter estimation and inference in conceptual rainfall- runoff modeling. Water Resour. Res 37 (4), 937–947.

Beven, K., Binley, A., 1992. The future of distributed models-model calibration and uncertainty prediction. Hydrological Processes 6 (3), 279–298.

Beven, K.J., Fisher, J.I., 1996. Remote sensing and scaling in hydrology. Stewart, J.B. (Ed.), Scaling Issues in Hydrology. Wiley:Chichester.

Bhave, A.G., Conway, D., Dessai, S., Stainforth, D.A., 2018. Water resource planning under future climate and socioeconomic uncertainty in the cauvery river basin in karnataka, india. Water Resour. Res. 54 (2), 708–728.

Birk, S., Geyer, T., Liedl, R., Sauter, M., 2005. Process-based interpretation of tracer tests in carbonate aquifers. Ground Water 43 (3), 381–388.

Bittner, D., Narany, T.S., Kohl, B., Disse, M., Chiogna, G., 2018. Modeling the hydrological impact of land use change in a dolomite-dominated karst system. J. Hydrol. 567, 267–279.

Cao, M., 2012. Effects of Urbanization on Hydrogeochemical and Stable Isotopic Characteristics of Karst Groundwater-A Case from the Laolongdong Watershed of Chongqing. Southwest University, Chongqing, China.

Chen, Y.B., 2009. Liuxihe Model. China Science and Technology Press, Beijing, China.

Chen, Y., Li, J., Xu, H., 2016. Improving flood forecasting capability of physically based distributed hydrological models by parameter optimization. Hydrol. Earth Syst. Sci. 20, 375–392. https://doi.org/10.5194/hess-20-375-2016.

Chen, Y., 2018. Distributed Hydrological Models., 2018. Springer Berlin Heidelberg, Switzerland. https://doi.org/10.1007/978-3-642-40457-3_23-1.

Choi, J., Harvey, J.W., Conklin, M.H., 1999. Use of multi-parameter sensitivity analysis to determine relative importance of factors influencing natural attenuation of mining contaminants. the Toxic Substances Hydrology Program Meeting, Charleston ,south Carolina.

Cornaton, F., Perrochet, P., 2002. Analytical 1D dual-porosity equivalent solutions to 3D discrete-continuum models. Application to karstic spring hydrograph modelling. J. Hydrol. 262, 165–176.

Dewandel, B., Lachassagne, P., Bakalowicz, M., Weng, P., Al-Malki, A., 2003. Evaluation of aquifer thickness by analysing recession hydrographs. Application to the Oman ophiolite hard-rock aquifer. J. Hydrol. 274 (1), 248–269.

Fan, Z., Hao, Z., Chen, Y., Wang, J.H., Huang, F.H., 2012. The Application and Research of Income Flood Simulation of the Baipenzhu Reservoir with the Liuxihe Model. Acta Scientiarum Naturalium Universitatis Sunyatseni 51 (2), 113–118.

Fleury, P., Plagnes, V., Bakalowicz, M., 2007. Modelling of the functioning of karst aquifers with a reservoir model: Application to Fontaine de Vaucluse (South of France). J. Hydrol. 345 (1–2), 38–49.

Frumkin, H., 2002. Urban sprawl and public health. Publ. Health Reports 117 (3), 201–217.

Geyer, T., Birk, S., Liedl, R., Sauter, M., 2008. Quantification of temporal distribution of recharge in karst systems from spring hydrographs. J. Hydrol. 348 (30), 452–463.

Glass, O., Guerrero, S., 2010. Controllability of the Korteweg-de Vries equation from the right Dirichlet boundary condition. Syst. Control Lett. 59 (7), 390–395.

Hartmann, A., Goldscheider, N., Wagener, T., Lange, J., Weiler, M., 2014. Karst water resources in a changing world. Review of hydrological modeling approaches. Rev. Geophys. 52 (3), 218–242.

Hartmann, A., Mudarra, M., Marín, A., Andreo, B., Wagener, T., 2015. Relating Land Surface Information and Model Parameters for a Karst System in Southern Spain. In: Hydrogeological and Environmental Investigations in Karst Systems Environmental Earth Sciences 1. Springer, Berlin, Heidelberg, pp. 345–352.

Kraller, G., Warscher, M., Strasser, U., Kunstmann, H., Franz, H., 2014. Distributed hydrological modeling and model adaption in high alpine karst at regional scale (berchtesgaden alps, germany). Springer Int. Publ. Switzerland. https://doi.org/10.1007/978-3-319-06139-9_8.

Lan, J.C., 2014. Study on Migration, Partitioning and Ecological Risk of PAHs in a Karst Underground River System in Southwest China. Southwest University, Chongqing, China.

Li, J., Chen, Y., Wang, H., Qin, J., Li, J., Chiao, S., 2017. Extending flood forecasting lead time in a large watershed by coupling WRF QPF with a distributed hydrological model. Hydrol. Earth Syst. Sci. 21, 1279–1294. https://doi.org/10.5194/hess-21-1279-2017.

Li, J., Yuan, D., Liu, J., Jiang, Y., Chen, Y., Hsu, K.L., Sorooshian, S., 2019a. Predicting floods in a large karst river basin by coupling PERSIANN-CCS QPEs with a physically based distributed hydrological model. Hydrol. Earth Syst. Sci. 23, 1505–1532.

Li, J., Hong, A., Yuan, D., Jiang, Y., Deng, S., Cao, C., Liu, J., Chen, Y., 2019b. Comparing the performances of WRF QPF and PERSIANN-CCS QPEs in karst flood simulations and forecasting with a new Karst-Liuxihe model. Hydrol. Earth Syst. Sci. Discuss. 1–48. https://doi.org/10.5194/hess-2019-285.

Liedl, R., Sauter, M., Huckinghaus, D., Clemens, T., Teutsch, G., 2003. Simulation of the development of karst aquifers using a coupled continuum pipe flow model. Water Resour. Res. 39 (3), 1057–1068. https://doi.org/10.1029/2001WR001206.

McMahon, P.B., Burow, K.R., Kauffman, L.J., Eberts, S.M., Böhlke, J.K., Gurdak, J.J., 2008. Simulated response of water quality in public supply wells to land use change. Water Resour. Res. 44 (7). https://doi.org/10.1029/2007WR006731.

Meng, H.H., Wang, L.C., Su, W.C., Huo, Y., 2009. Development of a Karst Sinkhole -based Semi-Distributed Hydrological Model and Its Application. Sci. Geographica Sinica 29 (4), 550–554.

Meyer, W.B., Turner, B., 1994. Change in land use and cover: A global perspective. Cambridge University Press, London.

Neuman, S.P., Elizabeth, A.J., 1984. Analysis of nointrinsic spatial variability by residual kriging with application to regional groundwater levels. J. Int. Assoc. Mathem. Geol. 16 (5), 499–521.

Nikolaidis, N.P., Bouraoui, F., Bidoglio, G., 2013. Hydrologic and geochemical modeling of a karstic Mediterranean watershed. J. Hydrol. 477, 129–138.

Rao, Y., 2005. The effects of Land Use on Kasrt Water Quality in Karst Regions. Doctoral dissertation, Southwest China Normal University, China.

Reimann, T., Hill, M.E., 2009. MODFLOW-CFP: A New Conduit Flood process for MODFLOW-2005. Ground Water 43, 321–325.

Sarrazin, F., Hartmann, A., Pianosi, F., Rosolem, R., Wagener, T., 2018. V2karst v1.1: a parsimonious large-scale integrated vegetation–recharge model to simulate the impact of climate and land cover change in karst regions. Geosci. Model Develop. 11 (12), 4933–4964.

Shuster, E.T., White, W.B., 1971. Seasonal fluctuations in the chemistry of lime-stone springs: A possible means for characterizing carbonate aquifers. J. Hydrol. 14 (2), 93–128.

Teutsch, G., Sauter, M., 1998. Distributed parameter modelling approaches in karst-hydrological investigations. Bull. d'Hydrogéologie 16, 99–109.

Trcek, B., Veselic, M., Pezdic, J., 2006. The vulnerability of karst springs-a case study of the Hubelj spring (SW Slovenia). Environ. Geol. 49 (6), 865–874.

Turner, B.L., Kasperson, R.E., Meyer, W.B., Dow, K.M., Golding, D., Kasperson, J.X., Ratick, S.J., 1990. Two types of global environmental change: definitional and spatial-scale issues in their human dimensions. Global Environ. Change 1 (1), 14–22.

Yuan, D.X., 2002. China karst power systems. Geological Publishing House, Beijing, China.

Zhang, Y.Z., 2017. Effects of allogenic acids (sulfuric acid and nitric acid) on karst carbon cycle-a study from Laolongdong subterranean catchment. Southwest University, Chongqing, China, Chongqing.

Zhang, J., Lin, G., Li, W., Wu, L., Zeng, L., 2018a. An Iterative Local Updating Ensemble Smoother for Estimation and Uncertainty Assessment of Hydrologic Model Parameters With Multimodal Distributions. Water Resour. Res. 54 (3), 1716–1733.

Zhu, C., Li, Y., 2014. Long-Term Hydrological Impacts of Land Use/Land Cover Change From 1984 to 2010 in the Little River Watershed, Tennessee. Int. Soil Water Conserv. Res. 2 (2), 11–21.

Zhang, S., Yang, Y., Mcvicar, T.R., Yang, D., 2018b. An analytical solution for the impact of vegetation changes on hydrological partitioning within the budyko framework. Water Resour. Res. 54 (1), 519–537.

Zhang, Z.C., Chen, X., Shi, P., Wei, L.N., 2009. Distributed hydrological model and eco-hydrological effect of vegetation in Karst watershed. Adv. Water Sci. 20, 6, 54–59.